ChemComm

COMMUNICATION

View Article Online
View Journal | View Issue

Cite this: *Chem. Commun.*, 2014, 50, 12201

Received 26th June 2014,
Accepted 11th August 2014

DOI: 10.1039/c4cc04887c

www.rsc.org/chemcomm

Nitrogen-doped carbon–graphene composites enhance the electrocatalytic performance of the supported Pt catalysts for methanol oxidation†

Jianbing Zhu,[ab] Meiling Xiao,[ab] Xiao Zhao,[ab] Kui Li,[bc] Changpeng Liu[c] and Wei Xing*[ac]

A novel nitrogen doped carbon–graphene support for a direct methanol fuel cell was synthesised *via* thermal decomposition of the graphene oxide–polypyrrole composite. The supported catalysts show considerable enhancement of activity and stability towards the methanol electrooxidation reaction. Physical characterizations reveal that the enhanced performance was due to a uniform particle dispersion and modified electronic structure of platinum nanoparticles by the support.

The rapid increase in energy demands, greenhouse gas emissions, and depletion of fossil fuels unquestionably make direct methanol fuel cells (DMFCs) an attractive technology due to their highly efficient fuel utilization and environmentally-friendly operation.[1–5] Although great progress has been made, there are still two major technical challenges hindering commercialization: insufficient reliability/durability and high cost.[6] One way to increase the durability and lower the cost is to enhance the utilization of the supported Pt or Pt alloy catalysts by the strong interaction/synergies between the catalysts and supports. To this end, the exploration of an advanced catalyst support is a promising route to obtain highly active and durable electrocatalysts.[7–10] Recently, graphene sheet (GS) has been regarded as a promising support for electrocatalysts due to its unique properties, such as ultrahigh theoretical surface area ($\sim$2630 m^2 g^{-1}), sufficient porosity, superior electron conductivity and rich surface chemistry.[11] However, previous research has shown that the actual performances of graphene-based supports are obviously depressed by the restacking phenomenon of reduced grapheme oxide (RGO). RGO tends to form an irreversible aggregation because of strong van der Waals interactions among individual reduced graphene sheets.[12] Since the physico-chemical properties of aggregated RGO are similar to graphite, the aggregated RGO not only ruins the advantage of an ultrahigh surface area but also obstructs the dispersion of electrocatalysts. Therefore, how to effectively minimize the restacking effect of RGO and to enhance the exposure of RGO are crucial issues in developing graphene-based supports.[13]

Herein, we exploited an effective two-step method to fabricate a 2D nano-structure hybrid with PPy decorated on the GO. Scheme 1 shows a schematic illustration of the composite preparation. PPy was first uniformly coated onto the GO sheets *via in situ* polymerization of pyrrole in the ethanol–water system. The products were marked as GO-X (X is the proportion of pyrrole/GO). Then the GO-X 2D nanostructure was annealed for one hour in a tube furnace at target temperatures yielding products denoted as GP-X-*T* (*T* is the annealing temperature). During heat-treatment, the GO was reduced. Pt/GP-X-*T* catalysts with the Pt loading of 20% were prepared *via* the microwave-assisted polyol method in ethylene glycol solution.

The representative electron microscopic images of the as-prepared support and catalysts are shown in Fig. 1 and Fig. S2 (ESI†). After being decorated by PPy, the GO sheets maintain their 2D nanosheet morphology, while numerous PPy particles homogeneously array themselves along the radial direction of a GO sheet (Fig. 1a). From the TEM images in Fig. 1b and Fig. S3–S5 (ESI†), it can be seen that the Pt nanoparticles are homogeneously deposited onto the GP-X-*T* supports with a narrow distribution. The average sizes of the Pt/GP-20-800 catalysts were estimated to be 3.0 nm according to the size-distribution histograms, which was the smallest among all the Pt/GP-X-*T* catalysts. The typical HRTEM

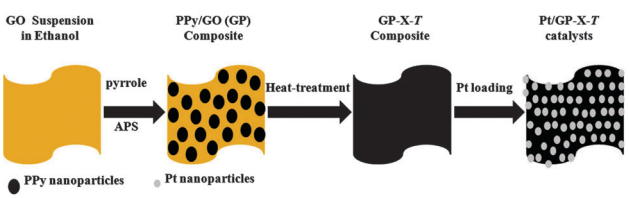

Scheme 1 Schematic view of the synthesis of the Pt/GP-X-*T* catalysts.

[a] State Key Laboratory of Electroanalytical Chemistry, Changchun Institute of Applied Chemistry, Chinese Academy of Sciences, Changchun, Jilin, 130022, China. E-mail: xingwei@ciac.jl.cn; Fax: +86-431-85685653; Tel: +86-431-85262223

[b] Graduate School of the Chinese Academy of Sciences, Beijing, 100039, China

[c] Laboratory of Advanced Power Sources, Changchun Institute of Applied Chemistry, 5625 Renmin Street, Changchun, 130022, P. R. China

† Electronic supplementary information (ESI) available: Materials used experimental details, and additional data. See DOI: 10.1039/c4cc04887c

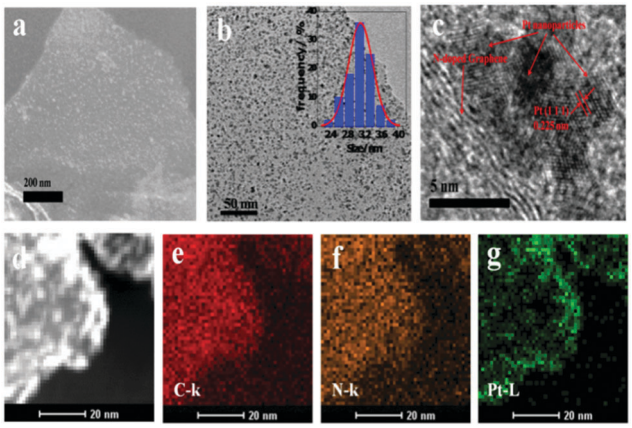

Fig. 1 SEM image of the as synthesized GP-20 (a) and TEM images of the Pt/GP-20-800 catalyst (b–d), and the EDS mapping images of the catalyst (e–g).

image (Fig. 1c) of the Pt/GP-20-800 catalyst shows well resolved ordered fringes of graphene and Pt(111) face. The high angle annular dark-field scanning TEM (HAADF-STEM) image displayed in Fig. 1d further confirmed the homogeneous deposition of Pt nanoparticles. The energy-dispersive X-ray spectroscopy (EDS) mapping profile shown in Fig. 1e–g obviously manifested the homogenous distribution of nitrogen and platinum in the Pt/GP-20-800 catalyst (Scheme 1).

The crystalline structures of the Pt/GP-X-*T* catalysts were investigated using powder X-ray diffraction (XRD) as shown in Fig. S2 (ESI†). All catalysts exhibit typical diffraction peaks of platinum with a face-centered cubic (fcc) structure with peaks located at the 2θ values of *ca.* 40°, 47°, 68°, and 82°, which can be indexed to the (111), (200), (220) and (311) diffractions of a face-centred-cubic (fcc) structure. The broad diffraction peak at *ca* 25° corresponds to the (002) plane of carbon. Next we tested the as-synthesized catalysts in the electrocatalytic reaction and compared them with the commercial Pt/C catalyst. Fig. 2; Fig. S6 and S7 and Table S1 (ESI†) detail the cyclic voltammograms (CVs) of catalysts in 0.5 M H_2SO_4 + 1 M MeOH. The activities of catalysts were normalized to the mass of Pt. It clearly shows that the forward peak current densities (J_f) are on the order of Pt/GP-20-800 > Pt/GP-50-800 > Pt/GP-10-800 > Pt/GP-20-700 > Pt/GP-20-900 ≈ Pt/GP-200-800 > Pt/C-JM. Especially, the Pt/GP-20-800 catalyst shows the superior catalytic activity with a forward peak current density of 603 mA mg_{Pt}^{-1}, 2.6 times that of commercial Pt/C-JM (231 mA mg^{-1}).

The stability is one of the critical factors required for a practical catalyst. To evaluate the stability of the catalysts, the chronoamperometric (CA) measurements of the catalysts were carried out in 0.5 M H_2SO_4 + 1 M MeOH solution at 0.5 V *vs.* SCE (Fig. 2c). Considering the different initial current values of the catalysts, the current was further normalized to the initial current to compare the stability. It is observed that the final current density of commercial Pt/C drops to almost 31.6% after a 3600 s stability test. Strikingly, the Pt/GP-20-800 catalyst shows small loss of current density after 3600 s, with an 86.4% current density remaining (shown in Fig. 2d). This is strong evidence to support that Pt/GP-20-800 has a better stability than commercial Pt/C. From the above results Pt/GP-20-800 manifested a superior catalytic performance to the commercial Pt/C catalyst for MOR; the as-prepared GP-20-800 composite represents an excellent support and can be present in other electrocatalytic actions and energy-related devices such as supercapacitors. For the superior performance of Pt/GP-20-800, the investigation for surface composition and electronic structure provides some clues. According to XPS patterns, (see Fig. 3 and Fig. S7, (ESI†)), Pt 4f signals for both catalysts can be deconvolved into two pairs of doublets which can be attributed to metallic Pt(0) (*ca.* 70.5 eV and 73.9 eV) and Pt(II) in the PtO or $Pt(OH)_2$ species (*ca.* 71.3 eV and 74.8 eV). The deposition of Pt NPs on GP-X-*T* support shifted the BEs of Pt 4f to slightly higher values. Specifically, a positive shift for Pt/GP-20-800 was detected compared to the Pt/C-commercial catalyst. Considering the similar morphology and particle size of Pt NPs in Pt/GP-20-800 and Pt/C-commercial catalysts, the positive shift in the BEs of Pt 4f for Pt/GP-20-800 catalyst is probably due to the metal–support interaction. The local N-doped carbon can modify the electronic structure of Pt leading to a lower density of states at the Fermi level, and reduce the Pt–CO band energy and weaken the CO adsorption on Pt.[14,15] From the deconvolved high-resolution N1s signals (Fig. S9 (ESI†)) the N 1s spectrum in GP-X-*T* can be

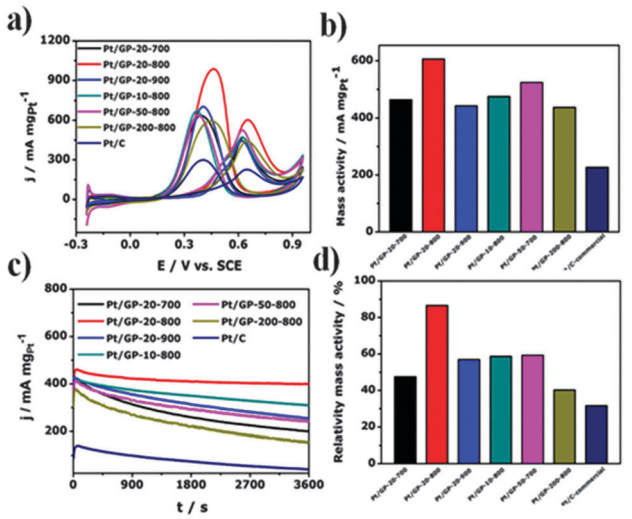

Fig. 2 The comparison of mass activity (a, b), stability (c) and relative stability (d) between Pt/GP-X-*T*, Pt/C-JM electrodes for MOR. The stability tests were conducted at a potential value of 0.5 V *vs.* SCE.

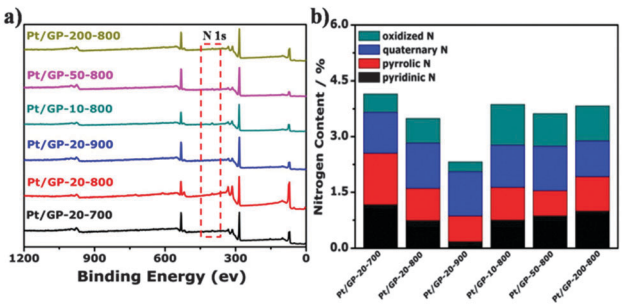

Fig. 3 XPS spectra and N content of the synthesis catalysts.

deconvolved into three N-based bonding configurations including pyridinic N (398.2 eV), pyrrolic N (399.7 eV), quaternary N (401.7 eV) and oxidized N (402.4 eV).[16–18] Upon nitrogen doping, the surface nanostructure of carbon materials change subtly. As the pyridinic and quaternary N replace the carbon atoms at the edge and interior of the graphene, respectively, and form C–N functionalities, these C–N functionalities can serve as active sites for anchoring Pt seeds onto the carbon surface. Also the increased electron density of nitrogen doping sites on graphitic carbon layers lead to stronger interactions between metal particles and supports in Pt/GP-X-*T* catalysts. So the Pt/GP-X-*T* shows a much higher activity and durability towards MOR. The higher content of pyridinic and quaternary N in the GP-20-800 support (Fig. 3a) could account for its highest activity and durability among all catalysts. Also, it is noteworthy that a further increase in the content of PPy (from GO : Py = 1 : 20 to 1 : 50 and 1 : 200) could not result in a continual increasing activity towards methanol electrooxidation; this may be because the increased PPy would enhance the disorder composite of the carbon materials, as shown in the Raman spectra (Fig. S10 and Table S3, ESI†), thus lowering the conductivity and durability of the GP-X-*T* supports, and this would lead to the decreased activity and stability during methanol electrooxidation. As for the Pt/GP-10-800 catalyst the poor performance towards MOR may be ascribed to the poor dispersion and the aggregation of Pt nanoparticles (Fig.S6, ESI†).

In conclusion, novel nitrogen doped carbon–graphene support supports were successfully fabricated by the *in situ* polymerization of pyrrole on graphene oxidation sheets followed by heat-treatment. Pt NPs supported on the GP-X-*T* show uniform and narrow dispersion. The Pt/GP-20-800 catalyst exhibits the best activity and durability compared to other catalysts. This enhancement originates from the beneficial effects of the GP-20-800 support. Its N-doped carbon–graphene structure helps to disperse and modify the electronic structure of the Pt NPs to improve the intrinsic kinetics of the methanol oxidation reaction.

This work was supported by the High Technology Research Program (863 program, No. 2012AA053401) of the Science and Technology Ministry of China, the National Basic Research Program of China (973 Program, No. 2012CB932800 and 2012CB215500), General Programs of National Natural Science Foundation of China (21073180, 21011130027), the Science & Technology Research Programs of the Jilin Province (20100420) and the Recruitment Program of Foreign Experts (WQ20122200077).

Notes and references

1 X. Zhao, M. Yin, L. Ma, L. Liang, C. P. Liu, J. H. Liao, T. H. Lu and W. Xing, *Energy Environ. Sci.*, 2011, **4**, 2736–2753.
2 H. Liu, C. Song, L. Zhang, J. Zhang, H. Wang and D. P. Wilkinson, *J. Power Sources*, 2006, **155**, 95–110.
3 D. S. Yuan, S. Z. Tan, Y. L. Liu, J. H. Zeng, F. P. Hu, X. Wang and P. K. Shen, *Carbon*, 2008, **46**, 531–536.
4 H. Tong, H. L. Li and X. G. Zhang, *Carbon*, 2007, **45**, 2424–2432.
5 I. S. Park, K. W. Park, J. H. Choi, C. R. Park and Y. E. Sung, *Carbon*, 2007, **45**, 28–33.
6 R. Borup, J. Meyers, B. Pivovar, Y. S. Kim, R. Mukundan, N. Garland, D. Myers, M. Wilson, F. Garzon and D. Wood, *Chem. Rev.*, 2007, **107**, 3904–3951.
7 E. Antolini, *Appl. Catal., B*, 2009, **88**, 1–24.
8 J. Salgado, R. Duarte, L. Ilharco, A. Botelho do Rego, A. Ferraria and M. Ferreira, *Appl. Catal., B*, 2011, **102**, 496–504.
9 B. Choi, H. Yoon, I. S. Park, J. Jang and Y. E. Sung, *Carbon*, 2007, **45**, 2496–2501.
10 W. Q. Yang, S. H. Yang, J. S. Guo, G. Q. Sun and Q. Xin, *Carbon*, 2007, **45**, 397–401.
11 M. J. Allen, V. C. Tung and R. B. Kaner, *Chem. Rev.*, 2010, **110**, 132–145.
12 H. Bai, C. Li and G. Q. Shi, *Adv. Mater.*, 2011, **23**, 1089–1115.
13 Y.-S. Wang, S.-Y. Yang, S.-M. Li, H.-W. Tien, S.-T. Hsiao, W.-H. Liao, C.-H. Liu, K.-H. Chang, C.-C. M. Ma and C.-C. Hu, *Electrochim. Acta*, 2013, **87**, 261–269.
14 X. Zhao, J. Zhu, L. Liang, J. Liao, C. Liu and W. Xing, *J. Mater. Chem.*, 2012, **22**, 19718–19725.
15 N. Dimakis, N. E. Navarro, T. Mion and E. S. Smotkin, *J. Phys. Chem. C*, 2014, **118**, 11711–11722.
16 X. Y. Tao, X. B. Zhang, F. Y. Sun, J. P. Cheng, F. Liu and Z. Q. Luo, *Diamond Relat. Mater.*, 2007, **16**, 425–430.
17 H. Liu, Y. Zhang, R. Li, X. Sun, S. Désilets, H. Abou-Rachid, M. Jaidann and L.-S. Lussier, *Carbon*, 2010, **48**, 1498–1507.
18 Y. Chen, J. Wang, H. Liu, M. N. Banis, R. Li, X. Sun, T.-K. Sham, S. Ye and S. Knights, *J. Phys. Chem. C*, 2011, **115**, 3769–3776.